



Element-Free Galerkin modelling of composite damage

I. Guiamatsia^{a,*}, B.G. Falzon^b, G.A.O. Davies^a, L. Iannucci^a

^a Imperial College London, Dpt. Aeronautics, Prince Consort Rd., South Kensington SW7 2AZ, UK

^b Monash University, Dpt. Mechanical and Aerospace Engineering, Building 31, Clayton Campus, VIC 3800, Australia

ARTICLE INFO

Article history:

Received 26 May 2009

Received in revised form 4 August 2009

Accepted 9 August 2009

Available online 18 August 2009

Keywords:

A. Polymer–matrix composites

C. Delamination

B. Matrix cracking

C. Meshless modelling

ABSTRACT

Delamination and matrix cracking are routine damage mechanisms, observed by post-mortem analysis of laminated structures containing geometrical features such as notches or bolts. Current finite element tools cannot explicitly model an intralaminar matrix microcrack, except if the location of the damage is specified *a priori*. In this work, a meshless technique, the Element-Free Galerkin (EFG) method, is utilized for the first time to simulate delamination (interlaminar) and intralaminar matrix microcracking in composite laminates.

© 2009 Elsevier Ltd. All rights reserved.

1. Introduction

In composite laminates, defects tend to accumulate at the interface between plies or in intralaminar pockets that are rich in resin. Consequently, interfaces and off-axis plies (worst case is a 90° ply with respect to the loading axis) are locations where cracks are likely to initiate. In realistic structures, both mechanisms of failure are usually present. With respect to finite element simulation, a smeared approach is usually adopted for the simulation of matrix cracking, while delamination is modelled discretely. This has notable shortcomings, as the very use of smearing effectively reduces the stress concentration that is needed to trigger a delamination driven by matrix cracking, Fig. 1.

Unfortunately, smearing is often the only option available, given that the location of the transverse crack may not be determined in advance, hence interface elements cannot always be used. Jiang et al. [1] used interface elements inserted transversely, following a failure path indicated by experimental results, however the aim of the current work is to develop truly predictive tools, including the determination of the propagation path as part of the problem's solution.

A previous investigation, Guiamatsia et al. [2], showed that a routine for inserting interface elements during the course of the simulation, implemented in a commercially available package, was computationally costly. On the other hand, meshless methods have existed for a number of years and the Element-Free Galerkin

(EFG) method was first proposed for the simulation of fracture 15 years ago, Belytschko et al. [3]. These methods offer the advantage of allowing topology changes – node creation, removal and ‘h’ refinement – in a seamless manner.

This paper is organized in three sections: first, a general description of the EFG method is provided, then the particular aspect of accuracy and convergence of meshless modelling of beams is examined. Finally, some results obtained for mixed-mode delamination, as well as matrix cracking are presented.

2. The Element-Free Galerkin method

A meshless method is defined in a broad sense as a method where nodes are not required to be interconnected. In the Element-Free Galerkin (EFG) method, a mesh of nodes is generated to define the domain and its boundaries, and the solution of the problem sought at these nodes. However, cells are also defined over the domain, and are referred to as background cells or integration mesh, used for numerical integration. Fig. 2 illustrates the concepts of a mesh of nodes and background mesh for a sample domain.

Two ingredients are essential for the numerical solution of a boundary-value problem based on a weak formulation: an interpolation scheme and a numerical integration scheme. In the finite element (FE) approach, both schemes directly derive from the element's definition, however in element-free modelling, special techniques are required. In the Element-Free Galerkin approach, the moving least squares (MLS) scheme is used for interpolation, and a mesh of background cells, with no required connection to the nodal discretization, is used for the purpose of numerical integration.

* Corresponding author. Tel.: +44 20 7594 5118; fax: +44 20 7584 8120.

E-mail addresses: i.guiamatsia@imperial.ac.uk, irene.guiamatsia@utoronto.ca (I. Guiamatsia).

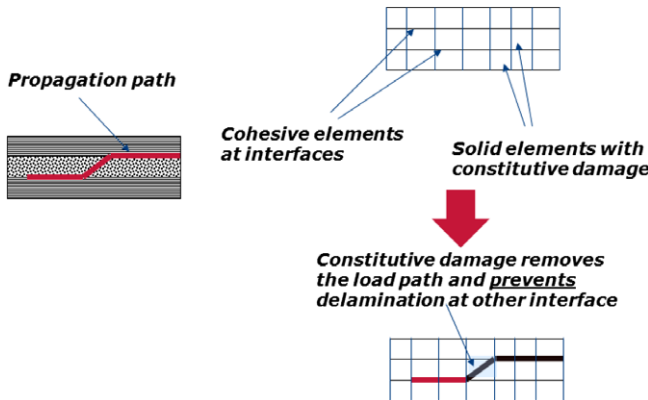


Fig. 1. Delamination triggered by transverse cracking.

A brief outline is presented in this paper but the reader is referred to the monograph by Liu [18] for further details.

2.1. MLS approximation

The moving least squares (MLS) interpolation is a data-fitting technique, Lancaster and Salkaukas [4], Nayroles et al. [5], and is at the heart of the EFG method's formulation. In this scheme, the least squares measure of the error is weighted in order to create a favorable bias for the neighborhood of the current function evaluation: the closer the point, the greater its influence on the interpolated value. The derivation presented here is limited to the one-dimensional case, for the sake of simplicity.

Consider a neighborhood, or support domain, of n nodes where the values of a function, $u_i = u(x_i)$, $i = 1, n$, are known. The unknown function, u , is approximated at an (integration) point of coordinate x using a basis of monomials $p^T = [1 \ x \ x^2 \ \dots \ x^m]$, where

$$u(x) \approx u^h(x) = p^T a = [1 \ x \ x^2 \ \dots \ x^m] \begin{Bmatrix} a_0(x) \\ a_1(x) \\ a_2(x) \\ \vdots \\ a_m(x) \end{Bmatrix}, \quad (1)$$

and m is the total number of monomials considered for the approximation. As a general rule, m is kept as small as possible, for instance $m = 2$, both to satisfy the condition: $m \ll n$, and to enable the determination of the vector of variable coefficients $a(x)$. These coefficients are given as the solution of the minimization of the least squares measure of the error J , where

$$J(x) = \sum_{i=1}^n [w(x - x_i)(p^T(x_i)a(x) - u_i)^2]. \quad (2)$$

The kernel or weight function, $w(x - x_i)$, is a bell shaped function that provides compactness to the interpolation, and also controls the degree of continuity of the resulting MLS interpolation. Commonly used kernel functions are the truncated gaussian, $w_g(d)$, the cubic spline, $w_{cs}(d)$ and quartic spline, $w_{qs}(d)$, where $d = \frac{|x-x_i|}{R}$ is the distance between the point where the function is evaluated and a support node i , and R is the radius of the support domain for the point of coordinate x ,

$$w_g(d) = \begin{cases} \frac{e^{-d-e^{-1}}}{1-e^{-1}} & \text{if } d \leq 1, \\ 0 & \text{if } d > 1, \end{cases} \quad (3)$$

$$w_{cs}(d) = \begin{cases} \frac{2}{3} - 4d^2 + 4d^3 & \text{if } d \leq \frac{1}{2}, \\ \frac{4}{3} - 4d + 4d^2 - \frac{4}{3}d^3 & \text{if } \frac{1}{2} < d \leq 1, \\ 0 & \text{if } d > 1, \end{cases} \quad (4)$$

$$w_{qs}(d) = \begin{cases} 1 - 6d^2 + 4d^3 - 3d^4 & \text{if } d \leq 1, \\ 0 & \text{if } d > 1. \end{cases} \quad (5)$$

The procedure for determining the radius R of the support domain is the following:

1. A radius of influence c is assigned to all nodes of the domain. This is usually either a fixed radius, or is determined from the smallest polygon surrounding the node, as suggested in Belytschko et al. [3].
2. All n nodes for which the current (integration) point x is within the radius of influence constitute the support domain of x .
3. Finally, the radius of the support domain is calculated as the largest distance between x and the support nodes:

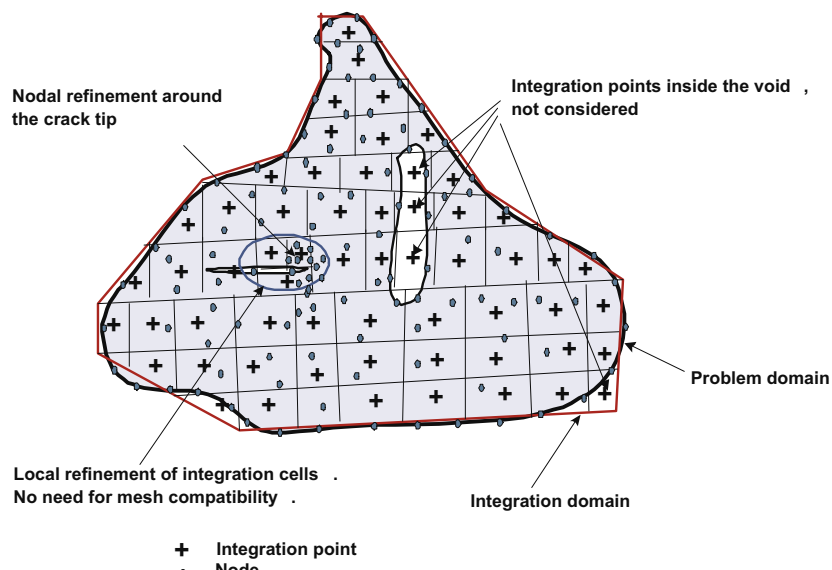


Fig. 2. Background mesh of integration cells for the EFG method.

$$R = \max(\|x - x_i\|), \quad \text{for } i = 1, n. \quad (6)$$

If a coordinate $x = x_0$ is chosen, setting $\frac{\partial f(x_0)}{\partial a_i(x_0)} = 0$ yields a system of n linear equations with n unknown coefficients $a_i(x_0)$:

$$A(x_0)a(x_0) = B(x_0)U, \quad (7)$$

$$A(x_0) = \sum_{i=1}^n w(x_0 - x_i) [p(x_0) p^T(x_0)], \quad U = \{u_1 \ u_2 \ \dots \ u_n\}^T,$$

$$B(x_0) = [w(x_0 - x_1)p(x_1) \ w(x_0 - x_2)p(x_2) \ \dots \ w(x_0 - x_n)p(x_n)].$$

The ‘moving’ character of the interpolation comes from the fact, outlined here, that these coefficients are only valid at point x_0 and will be different, in general, for any other point of coordinates $x \neq x_0$. Substituting the values of the coefficients in the initial approximation yields the shape functions, i.e. the vector of weights corresponding to each node of the support domain,

$$u(x) = \phi(x)U \Rightarrow \phi(x) = p(x)A^{-1}(x)B(x). \quad (8)$$

The derivatives of the shape functions are calculated simultaneously in the same routine using Eq. (9), where the dependence on the variable x is omitted here for clarity of the presentation,

$$\phi_x = \frac{\partial \phi}{\partial x} = (p_x - pA^{-1}A_x)A^{-1}B + pA^{-1}B_x. \quad (9)$$

2.2. Equilibrium equations

The Galerkin weak form is formulated in a general manner, making use of Lagrange multipliers for the imposition of Dirichlet-type boundary conditions and can be found in classical references such as Zienkiewicz and Taylor [8] and Bathe [9].

Given the equilibrium equations within the domain, Ω , of the problem,

$$\nabla \cdot \sigma + \mathbf{b} = 0 \quad \sigma_{ij}n_j = t_j|_{\Gamma_t} \quad u_i = u_{i0}|_{\Gamma_u}, \quad (10)$$

$$\sigma = [\sigma_{ij}, i, j = x, y, z] = [\sigma_{xx} \ \sigma_{yy} \ \sigma_{zz} \ \sigma_{yz} \ \sigma_{xz} \ \sigma_{xy}]^T,$$

$$\mathbf{b} = [b_x \ b_y \ b_z]^T, \quad \mathbf{u} = [u_x \ u_y \ u_z]^T = [u \ v \ w]^T.$$

In Eq. (10), Γ_t is the boundary where natural constraints are enforced, Γ_u defines the boundary where essential displacement constraints are imposed and \mathbf{b} is the body force vector.

The weak form is written with Lagrange multipliers λ_i , $i = 1, n_e$ associated with the n_e essential boundary conditions, assuming the Einstein summation over repeated indices:

$$\int_{\Omega} \delta \epsilon^T \sigma d\Omega - \int_{\Omega} \delta u^T b d\Omega - \int_{\Gamma_t} \delta u_j^T t_j d\Gamma - \int_{\Gamma_u} \delta \lambda_i^T (u_i - u_{i0}) d\Gamma - \int_{\Gamma_u} \delta u_i^T \lambda d\Gamma = 0. \quad (11)$$

The Lagrange multipliers are required for the EFG formulation to pass the convergence patch test, Belytschko et al. [3], because the MLS shape functions are non-interpolating:

$$\phi_i(x_j) \neq \delta_{ij} \Rightarrow u^h(x_i) \neq u_i. \quad (12)$$

It should also be noted that the trial functions used for the multipliers, λ , are isoparametric Lagrange shape functions and not MLS shape functions, Belytschko et al. [3]; this guarantees that the constraint is enforced on the entire boundary Γ_u and not only at discrete nodes. The weak form is then integrated numerically over the domain, taking a sufficiently high order of quadrature, as a function of the size of the background cells and the nodal distribution.

3. Miscellaneous modelling issues

For the purpose of this study, modelling is done at the mesolevel, with each ply represented individually, with an orthotropic constitutive law. The background integration cells are arranged per layer, in such a manner that they are not traversed by material interfaces. This is to ensure that stress gradients across material interfaces are correctly captured. In addition, it was found to be efficient to have the basic nodal discretization coincide with the background integration cells in most of the domain, except for the neighborhood of discontinuities where additional nodes provide ‘h’ refinement.

The crack is represented by a set of connected linear segments stored during the analysis, although the level-set technique, Sukumar et al. [10], Ventura et al. [8], allows for more efficient book keeping in three-dimensional analysis, or when multiphase materials are considered, Hettich et al. [9]. The presence of the crack usually creates a sharp discontinuity of the MLS approximation, and methods such as diffraction or transparency, Belytschko and Fleming, [7], can attenuate this effect. In the cases examined, it is ensured that the nodal discretization always involves nodes on each side of the crack line, hence the visibility method is used, with minimal error, to construct the MLS interpolation for the vicinity of cracks. The application of the MLS interpolation/cell integration to the treatment of slender laminated structures brought forward several issues that are worthy of mention:

3.1. Tensor-product vs. radial kernels

The multidimensional kernel function can be based on the absolute distance between nodes, referred to as a radial kernel, or a tensor-product kernel which distinguishes between dimensions, Krystl and Belytschko [6]. The latter is used in this work, and as a general rule, in cases where the aspect ratio between longitudinal (x) and transverse (y) directions is higher than 10, different support lengths R_x and R_y are used, respectively.

Tensor-product kernel :

$$J(x, y) = \sum_{i=1}^n \left[w\left(\frac{x - x_i}{R_x}\right) w\left(\frac{y - y_i}{R_y}\right) (p^T(x_i, y_i) a(x, y) - u_i)^2 \right], \quad (13)$$

Radial kernel :

$$J(x, y) = \sum_{i=1}^n \left[w(d) (p^T(x_i, y_i) a(x, y) - u_i)^2 \right], \quad (14)$$

$$\text{with } d = \frac{\sqrt{(x - x_i)^2 + (y - y_i)^2}}{R}.$$

3.2. Nodal influence domain

The nodal radius of influence determines the region of the domain affected by each node and is used in selecting the support domain of a given quadrature point, as previously explained. Several methods for selecting this distance are available in the literature and the most common options are: the fixed radius, the third closest node, and the minimum polygon, which are detailed in Liu [18]. The need for a variable nodal radius of influence is clear in the transition between high and low density areas of the domain. Although, the third closest node is often chosen for simplicity, the minimum polygon is more robust, Fig. 3a.

In modelling composite laminates, the use of the terminology ‘lengths’ of influence is preferred as the domain of influence now has a rectangular shape. As shown in Fig. 3, the minimum polygon surrounding a node is used to determine the lengths of influence, R_x and R_y , corresponding to the longitudinal and transverse direc-

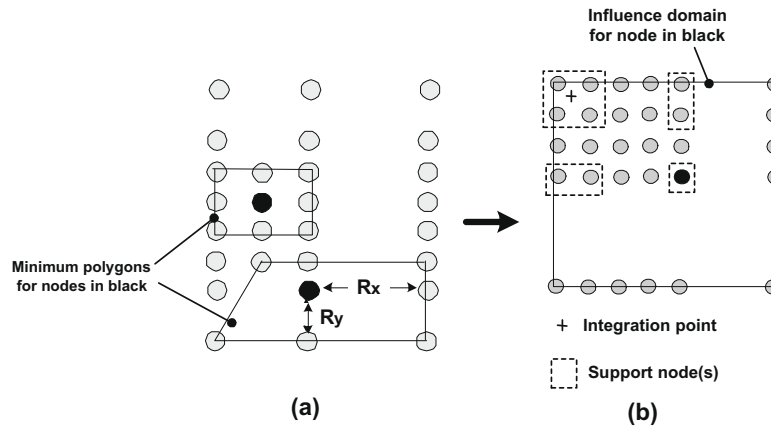


Fig. 3. Nodal influence domain. (a) Minimum polygon method. (b) Support nodes.

tions, respectively. However, this method can also be prone to numerical difficulties. In the situation represented in Fig. 3b, for instance, the node at the corner of the refinement zone has lengths of influence equal to its distance from the nodes to the right and below. Because that distance is large compared to the distance between nodes inside the refinement zone, that node on the corner is found to belong to the set of support nodes for the integration point shown with a plus sign. This results in the distance between the four nodes immediately surrounding the integration point being relatively insignificant – depending on the density of refinement – compared to the size of the support domain given by the largest distance between the point and the support nodes. Consequently, the value of the kernel, or weight function, at any of those four nodes is more or less the same, resulting in the singularity of the coefficient matrix A . The solution adopted was to define two lengths of influence per direction, per node, a total of four (left, right, top and bottom), Fig. 4.

Additionally, any refinement is performed throughout the entire thickness of the laminate, as shown in Fig. 5. This means a refinement along the longitudinal (x) direction only, which is sufficient for the problems examined here. Note that wherever refinement is applied, the order of the MLS shape functions increases (this means that, if the MLS shape functions were fitted with a polynomial, a higher order polynomial would be required), and it becomes necessary either to increase the order of numerical integration, or subdivide the background cells. The latter option was implemented in this work, as it is shown to be a more effective strategy, Dolbow and Belytschko [16]. It should also be noted that regular meshes were used throughout this work, they generally yield

greater accuracy than random, irregular meshes, especially if the order of monomials m utilized is low, Belytschko et al. [3].

3.3. Internal forces

The virtual crack closure technique (VCCT) was used here for crack advancement. The strain energy release rates in fracture modes I and II were calculated with a simple formula involving the internal forces at the crack tip, Rybicki and Kanninen [15]. The technique is particularly well suited for a finite element mesh, as the required forces are exactly the internal reactions obtained by multiplying the element stiffness matrix by the displacement solution.

Since there is no association between background integration cells and nodes in the EFG method, a simple and accurate way of finding the sought forces was to split the crack tip into two nodes and insert a spring with a very high stiffness between them, Fig. 6. Gauss points lying on one side of the crack line were supported by one half of the tip node, while those on the other side are supported by the other half. The stiffness of the spring was made as large as possible, for instance

$$K_s = 1000 \max(K_{ij}). \quad (15)$$

Care should be taken to ensure that the distance between the two nodes at the crack tip remains insignificant throughout the analysis, in such a way that no extra strain energy is added to the system. This can be verified by computing the ratio of the strain energy stored within the spring ΔU_s (given in Eq. (16)) to the total

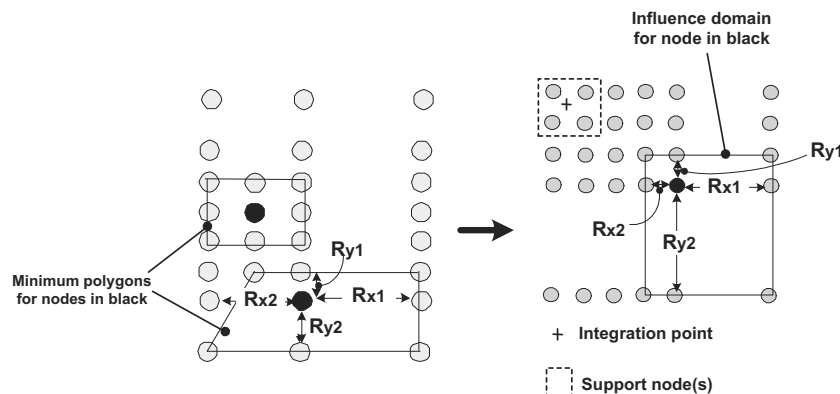


Fig. 4. Nodal influence with two influence lengths per direction.

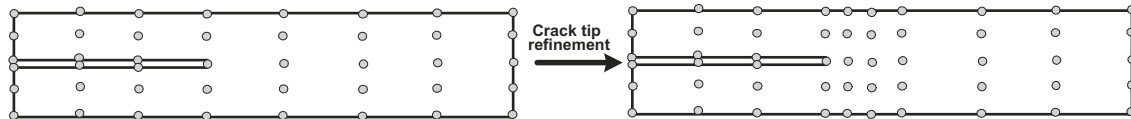


Fig. 5. Through thickness refinement.

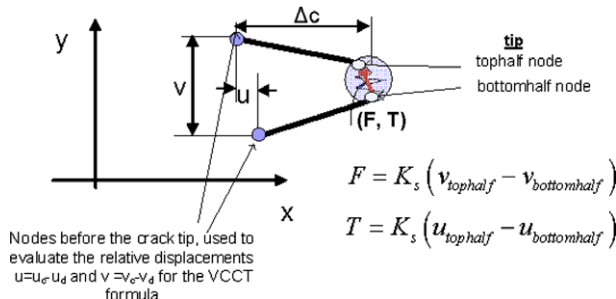


Fig. 6. Crack tip node splitting for internal reactions.

strain energy of the system.¹ The value of that ratio should be very small, less than 0.01% in order to ensure that no significant alteration of the structure results from the procedure.

$$\Delta U_s = \frac{1}{2} K_s (u_{tophalf} - u_{bottomhalf})^2 + \frac{1}{2} K_s (v_{tophalf} - v_{bottomhalf})^2. \quad (16)$$

Note that the value of 0.01% is only indicative and it suffices that the additional strain energy is ‘small enough’ as per the analyst’s judgment. It is also recommended to ensure that the additional strain energy due to the presence of the spring remains ‘small enough’, when the calculation is made for local area around the crack tip.

3.4. Shear locking

With the finite element approach, reduced integration is often used to address the issue of transverse shear locking in constant strain linear elements. Although MLS shape functions are in general not polynomials, it can be shown that for a rectangular integration cell containing a node at each corner, the use of a complete basis of monomials.

$$p = [1 \ x \ y \ xy], \quad (17)$$

yields MLS shape functions that are in fact identical to the isoparametric shape functions over that domain. As mentioned, the nodal discretization and the MLS shape functions are, in most of the domain, similar to finite elements (FE) approximations. Therefore using full integration here yields problems associated with shear locking, similar to the FE approach; issues related to membrane and volumetric locking are addressed by Krysl and Belytschko [12], Huerta and Fernandez-Mendez [13].

Reduced integration is effective for finite elements, because the shape of the interpolation over the integration domain (cf. the element) is known. Here, integration cells are independent of the nodes, and the idea cannot be applied to a meshless approach directly. Instead, Dolbow and Belytschko [14] found that a selective reduced integration scheme for nearly incompressible materials could be adapted for the meshless approach by using a nodal integration for the integration of the dilatational part of the stiffness matrix. The same concept can be applied to modelling slender

beams: the bending portion of the stiffness matrix is integrated using a regular (full) quadrature scheme over the integration cells, and the shear portion is integrated using nodal integration.

4. Results

The Element-Free Galerkin method was applied to several benchmarks of composite beam delamination, as well as the analysis of the microcracking of a constrained ply. It is worth mentioning that the parameters needed for a VCCT propagation, the displacements and internal forces, can be determined with excellent accuracy with very coarse meshes. Therefore a coarse nodal discretization suffices and refinement is utilized at the crack tip in order to achieve a smoother crack advancement.

4.1. Mixed-mode delamination

As mentioned, VCCT was used to determine crack advancement for all cases studied here. The mixed-mode interaction was modelled through the power law:

$$\left(\frac{G_I}{G_{Ic}}\right)^{\alpha} + \left(\frac{G_{II}}{G_{IIC}}\right)^{\alpha} = 1, \quad 1 \leq \alpha \leq 2. \quad (18)$$

A double cantilever beam (DCB), NAFEMS [17], a mixed-mode bending beam, Mi et al. [20] and a two-crack DCB problem, Robinson et al. [19] were considered; the properties and geometry details were as given in Figs. 7, 9, and 11. The simulations were performed with a nodal spacing in the transverse direction such that there were a minimum of three nodes through the thickness of each half beam.

4.1.1. Double cantilever beam [17]

The double cantilever beam test is a pure mode I crack propagation test. The specifications for the specimen illustrated in Fig. 7 are $a = 30$ mm, $L = 100$ mm, $h = 3$ mm and width $B = 20$ mm.

The discretization consisted of a uniform nodal spacing of 10 mm in the longitudinal (x) direction, and of 0.5 mm in the transverse direction. When the energy released, as calculated via VCCT, reached the fracture toughness, the crack was advanced by the smallest distance between nodes, here 10 mm. To perform smaller advancement steps (5 mm, 2 mm, 1 mm and 0.5 mm), local refinement was used around of the crack tip. The results obtained are reported as traction against separation plots, Fig. 8, and excellent

DOUBLE CANTILEVER BEAM			
$E_{II}=135.3$ GPa	$E_{22}=E_{33}=9.0$ GPa	$G_{I2}=5.2$ GPa	$G_{23}=3.269$ GPa
$v_{13}=v_{12}=-0.24$	$v_{23}=0.46$	$G_{el}=0.28$ N/mm	$G_{cl}=0.28$ N/mm

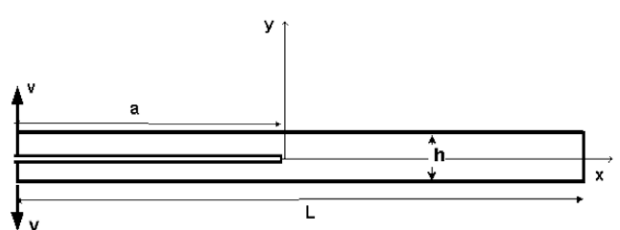


Fig. 7. Double cantilever beam: geometry and test setup.

¹ The total strain energy is also the work of external forces, and can be calculated easily by multiplying reaction forces and displacements at locations where loads are applied.

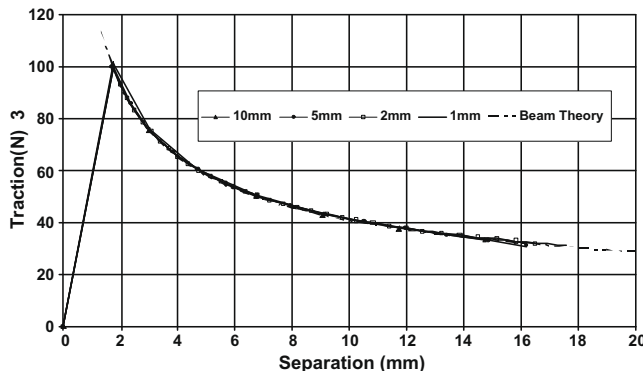


Fig. 8. Simulation of delamination in a double cantilever beam specimen, with various nodal spacing.

MIXED-MODE BENDING TEST			
$E=135.3 \text{ GPa}$	$\nu=0.29$	$G_{cr}=0.28 \text{ N/mm}$	$G_{cf}=0.28 \text{ N/mm}$
$L=50 \text{ mm}$	$c=43.72 \text{ mm}$	$a=30 \text{ mm}$	

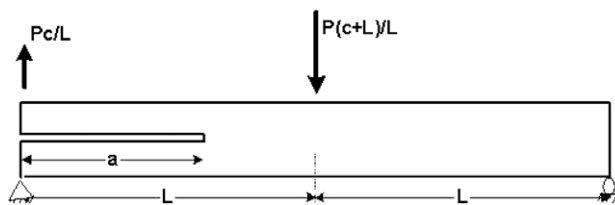


Fig. 9. Mixed-mode bending beam: geometry and test setup.

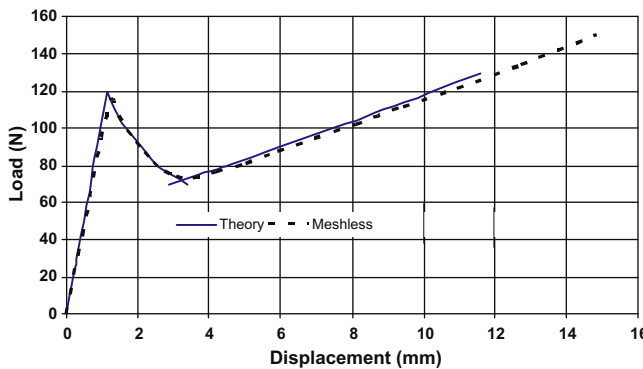


Fig. 10. Load vs. displacement – mixed-mode bending specimen.

agreement is found between the EFG and beam theory predictions. Note that with a large crack advancement – 10 mm – the propagation curve is not as smooth, however the correct force is predicted for the corresponding applied displacement.

4.1.2. Mixed-mode bending specimen

This specimen is designed in such a way that mode mixity can be controlled by the relative location of the points of application of loads. With the properties given in Fig. 9, the ratio between modes I and II is one. Note that Fig. 9 shows a ‘modelling’ geometry, indicating the resulting loads applied at two locations. In reality, the load is applied through a lever, featuring a distance c that can be modified to achieve different mode mixity ratios. The physical set-up can be found in Mi and Crisfield [20].

In the mixed-mode bending test, the crack propagates with a reduction in the applied load for $a < L$. For $a > L$, the propagation proceeds with a stiffening of the structure as witnessed by the increase in the applied load required to obtain the critical strain energy release rate G_c . The mesh consisted of 5 mm nodal spacing along the longitudinal axis, with a refinement of 1 mm near the crack tip; and 0.5 mm nodal spacing across the beam.

The EFG solution for this isotropic beam, Fig. 10, is, again, in excellent agreement with analytical solutions provided by Mi and Crisfield [20] for $a < L$, and Tenchev and Falzon [21] for $a > L$.

4.1.3. Two-crack DCB specimen

The two-crack DCB, Robinson et al. [19], Fig. 11, is a 24 ply standard double cantilever beam which also contains a secondary crack, inserted two plies below the main crack. This specimen first behaves as a typical DCB, with delamination of the main crack and softening of the entire structure as the main crack approaches to the secondary crack. The main crack moves dynamically over the second crack, but subsequent propagation leads to the general stiffening of the structure. Finally, both cracks propagate simultaneously, in a stable fashion, with the overall softening of the structure again.

The meshless discretization consisted of three rows of nodes – equivalent to two linear elements through the thickness in FE – for the lower 10 plies and the upper 12 plies. An additional two rows of nodes – equivalent to one linear element through the thickness in FE – are used for the ‘middle’ two plies. In the longitudinal direction, the uniform coarse discretization consisted of a nodal spacing of 5 mm. The refinement, within the 5 mm long region just ahead of each crack tip, consisted of a nodal spacing of either 0.5 mm. The results are shown in the form of a traction vs. separation plot, comparing the results obtained with EFG with predic-

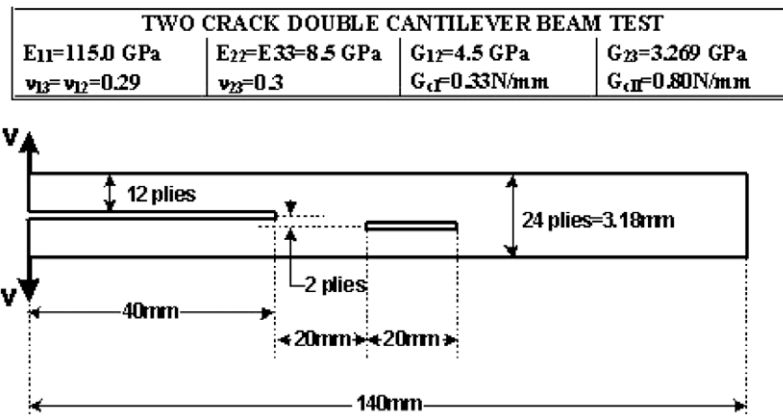


Fig. 11. Two-crack DCB: geometry and test setup.

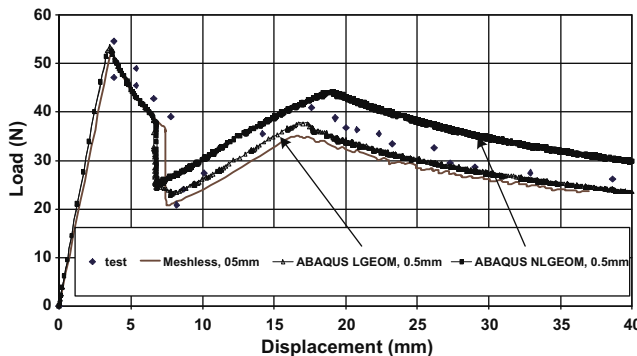


Fig. 12. Load vs. displacement – two-crack DCB.

tions from the FE commercial package ABAQUS/Standard, as well as experimental data, Robinson et al. [19], in Fig. 12.

Although the second phase of propagation involves simultaneous propagation of two crack fronts, one tip will generally reach the critical value of G_c before the other, hence it is helpful to advance the crack tip by small amounts, as well as reduce the time increment. It should also be mentioned that the current implementation does not account for geometric non-linearity, hence the curve corresponding to ABAQUS with linear geometry is most relevant for comparisons.

The initial and deformed meshless models for the three cases considered above are reported in Table 1.

4.2. Microcrack modelling

The EFG technique was finally used to simulate microcracking in a $(0^\circ, 90^\circ)_s$ laminate subjected to a uniform tensile load. Fig. 13 shows the cross-ply laminate considered, with zero degree, 0.5 mm thick, facesheets and 90°, 2 mm thick, core. A uniform tensile displacement is applied at one end of the beam and a simply supported boundary condition at the other.

The initial stress distribution in the off-axis (90°) layer is uniform in the far-field where the symmetry condition is applied, and increases near the point of application of the load. A new crack is inserted if the stress is higher than the strength, and is also a local maximum. Fig. 14 shows the deformed shape of the beam, focused at two locations along the beam (x axis is position along the beam) in order to highlight the location of cracks, where vertical

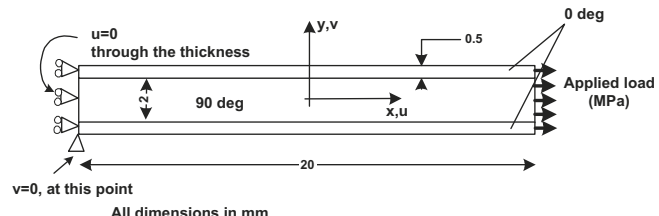


Fig. 13. Model for the microcrack analysis.

cal lines were inserted for more clarity. Fig. 15 plots the stress profile in the off-axis layer, along the beam. As expected, the stress varies from zero at the crack to a maximum at a location approximately half-way between two cracks. Both results correspond to an applied normal stress of 400 MPa.

5. Concluding remarks

In this work, mixed-mode delamination of laminated composite beams was simulated using the meshless Element-Free Galerkin (EFG) method. Tensor weighting kernels in the moving least squares approximation and rectangular domains of influence were found to be appropriate for the computation of trial functions for high geometrical aspect ratios.

It was shown that VCCT can be used for crack propagation in multiple cracked specimens, as long as cracks are advanced by sufficiently small steps. In the cases examined, the crack tip refinement is necessary in order to use small crack jumps in the VCCT implementation, which is shown to be critical for the two-crack DCB specimen. Using linear analysis, the results obtained were in good agreement with analytical or finite element predictions for the standard double cantilever beam and mixed-mode bending tests, as well as for a multiple delamination case. It is worth noting that the solution time for the delamination specimens is significantly lower than an equivalent finite element model using cohesive elements, because a linear solution is sought here.

It is also understood that, precisely because of the aspect ratio argument, the introduction of geometrical non-linearities – full deformation gradients – might mean the use of radial kernels, which requires discretizations in both x and y directions to be approximately of the same level of refinement. This would translate into significantly higher number of degrees of freedom, possibly jeopardizing the cost-effectiveness of the meshless approach.

Table 1
Initial and deformed configurations.

Case	Initial	Deformed
DCB		
MMB		
Two-crack DCB		

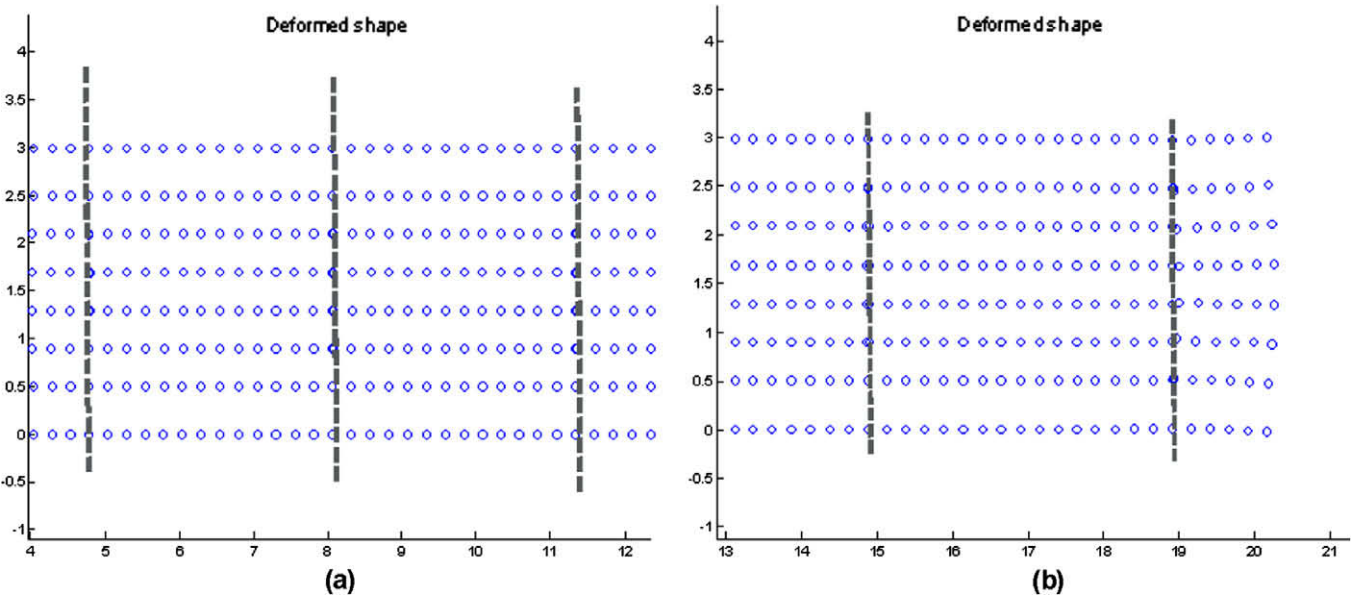


Fig. 14. Cracks distribution at 400 MPa.

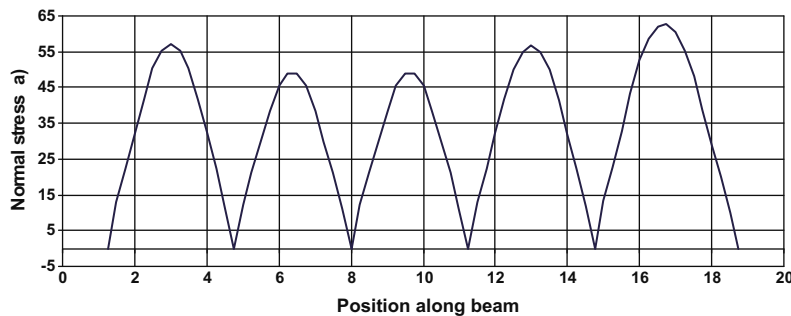


Fig. 15. Stress profile along the beam at 400 MPa.

Microcracking was also modelled separately, with results comparable to experimental and other analytical predictions. In this case, crack initiation was a simple operation of node creation, as opposed to the equivalent finite element approach. Both failure modes examined here are expected to be combined in further work, for the simulation of crack migration between interfaces, as this type of failure is routinely observed in component tests, near geometrical features.

Acknowledgements

This work is part of a project looking at the development of unified numerical approaches for the analysis of damage in composite structures with geometrical discontinuities. The joint support of EPSRC and DSTL through Grant EP/E023967/1, is gratefully acknowledged.

References

- [1] Jiang WG, Hallett SR, Green BG, Wisnom MR. A concise interface constitutive law for analysis of delamination and splitting in composite materials and its application to scaled notched tensile specimens. *Int J Numer Meth Eng* 2006;69:1982–95.
- [2] Guiamatsia I, Falzon BG, Davies GAO. Automatic insertion of cohesive elements for delamination modelling. *Key Eng Mater* 2008;383:53–66.
- [3] Belytschko T, Gu L, Lu YY. Fracture and crack growth by element-free Galerkin methods. *Modell Simulat Mater Sci Eng* 1994;2:519–34.
- [4] Lancaster P, Salkauskas K. Surfaces generated by moving least squares methods. *Math Comput* 1981;37:141–58.
- [5] Nayroles B, Touzot G, Villon P. Generalizing the finite element method: diffuse approximation and diffuse elements. *Comput Mech* 1992;10:307–18.
- [6] Krysl P, Belytschko T. ESFLIB: a library to compute the element free Galerkin shape functions. *Comput Meth Appl Mech Eng* 2001;190:2181–205.
- [7] Belytschko T, Fleming M. Smoothing, enrichment and contact in the element-free Galerkin method. *Comput Struct* 1999;71:173–95.
- [8] Ventura G, Xu JX, Belytschko T. A vector level set method and a new discontinuity approximations for crack growth by EFG. *Int J Numer Meth Eng* 2002;54:923–44.
- [9] Hettich T, Hund A, Ramm E. Modeling of failure in composites by X-FEM and level-sets within a multiscale framework. *Comput Meth Appl Mech Eng* 2008;197:414–24.
- [10] Sukumar N, Chopp D, Moes N, Belytschko T. Modeling holes and inclusions by level sets in the extended finite element method. *Comput Meth Appl Mech Eng* 2001;190:6183–200.
- [11] Krysl P, Belytschko T. Analysis of thin shells by the element-free Galerkin method. *Int J Solids Struct* 1996;33:3057–80.
- [12] Huerta A, Fernandez-Mendez S. Locking in the incompressible limit for the element free Galerkin method. *Int J Numer Meth Eng* 2001;51:1361–83.
- [13] Dolbow J, Belytschko T. Volumetric locking in the element free Galerkin method. *Int J Numer Meth Eng* 1999;46:925–42.
- [14] Rybicki EF, Kanninen EF. A finite element calculation of stress intensity factors by a modified crack closure integral. *Eng Fract Mech* 1977;9:931–8.
- [15] Dolbow JJ, Belytschko T. Numerical integration of the Galerkin weak form in meshfree methods. *Comput Mech* 1999;23(3):219–30.
- [16] Davies GAO. Benchmarks for composite delamination. *Benchmarks for composites*. Imperial College London: NAFEMS; 2002.
- [17] Liu GR. Meshfree methods: moving beyond the finite element method. Berlin: CRC Press; 2002. 692.
- [18] Robinson P, Besant T, Hitchings D. Delamination growth prediction using a finite element approach. In: 2nd ESIS TC4 conference on polymers and composites, Les Diablerets, Switzerland; 1999.

- [20] Mi Y, Aliabadi MH, Crisfield MA. Analytical derivation of load/displacement relationship for the DCB and MMB and proof of the FEA formulation. Imperial College London: Department of Aeronautics; 1996. 27 p.
- [21] Tenchev R, Falzon BG. A correction to the analytical solution of the mixed mode bending (MMB) problem. Compos Sci Technol 2007;67: 662–8.